Nanoscale

Accepted Manuscript

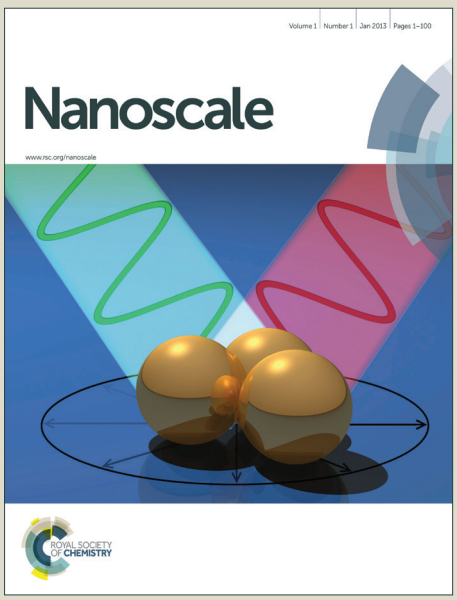

ROYAL SOCIETY OF CHEMISTRY

www.rsc.org/nanoscale

Journal Name

RSCPublishing

ARTICLE

Plasmon enhanced organic devices utilizing highly ordered nanoimprint gold nanodisks and nitrogen doped graphene

Cite this: DOI: 10.1039/x0xx00000x

Received 00th January 2012,
Accepted 00th January 2012

DOI: 10.1039/x0xx00000x

www.rsc.org/

Mohd Asri Mat Teridi,*[a] Mehran Sookhakian,[a] Wan Jefrey Basirun,[b] R. Zakaria,[b] Fabio Kurt Shneider,[c] Wilson Jose da Silva,*[c] Jaeyeon Kim,[d] Seung Joo Lee,[d] Hyeong Pil Kim,[d] Abd. Rashid bin Mohd Yusoff,*[d] and Jin Jang*[d]

High performance organic devices including polymer solar cells (PSCs) and light emitting diodes (PLEDs) were successfully demonstrated with the presence of highly ordered nanoimprint Au nanodisks (Au NDs) in their solution-processed active/emissive layers, respectively. PSCs and PLEDs were fabricated using a low bandgap polymer and acceptor, nitrogen doped multiwalled carbon nanotubes poly[4,8-bis[(2-ethylhexyl)oxy]benzo[1,2-b:4,5-b']dithiophene-2,6-diyl][3-fluoro-2-[(2-ethylhexyl)carbonyl] thieno[3,4-b]-thiophenediyl] (n-MWCNTs:PTB7), and [6,6]-phenyl C_{71} butyric acid methyl ester ($PC_{71}BM$) and (4,4-N,N-dicarbazole) biphenyl (CBP) doped with tris(2-phenylpyridine) iridium(III) ($Ir(ppy)_3$) as active/emissive layers, respectively. We synthesized nitrogen doped graphene and used as anodic buffer layer in both devices. The localized surface plasmon resonance (LSPR) effect from Au NDs clearly contributed to the increase in light absorption/emission in the active layers from electromagnetic field enhancement, which originated from the excited LSPR in PSCs and PLEDs. In addition to the high density of LSPR and strong exciton-SP coupling, the electroluminescent (EL) enhancement is ascribed to enhanced spontaneous emission rates. This is due to the plasmonic near-field effect induced by Au NDs. The PSCs and PLEDs exhibited 14.98% (8.08 to 9.29%) under one sun of simulated air mass 1.5 global (AM1.5G) illumination (100 mW/cm^2) and 19.18% (8.24 to 9.82 lm/W) enhancement in the power conversion efficiencies (PCEs), respectively, compared to the control devices without Au NDs.

1 Introduction

Today, organic/polymer solar cells (O/PSCs) have attracted voluminous researchers due to lightweight, cost-effective, non-toxic, mechanically flexible, and transparent [1]. Although research activities related to this device have started long ago, only recent a significant progress has been made, and today the power conversion efficiency (PCE) of OSCs has increased to nearly 12% [2]. In this device, we adopted 1+1+1 device configuration to fully exploit the capability of multi-junction with a complementary absorption spectrum in the near infra-red region. In addition, it has also been previously reported that multi-junction OSCs are able to overcome two major drawbacks in single-junction OSCs namely (i) thermalization of excited carriers and (ii) transmission of unabsorbed photons [3,4]. Despite the aforementioned issues, single-junction OSCs made a huge progress in the last few years, where Mitsubishi Chemical has announced an 11.1% PCE in their recent work [4].

On the other hand, polymer light emitting diodes (PLEDs) have also undergone significant progress in the past two decades [5]. They are attractive for new generations of low-cost novel solid state lighting and flat panel displays due to their unique advantages. These include flexibility, large area scalability, high power efficiency and a convenient solution based-fabrication process. Many efforts have been made to improve PLEDs performances and device lifetime including the synthesis of novel luminescent materials [6], the use of better multi-layer device architectures [7,8], and integration within hybrid organic–inorganic heterostructures [9,10]. Low fabrication cost is a key factor to allow large-scale PLEDs integration and mass-production.

Another interesting topic in organic devices, in particular organic/polymer solar cells (O/PSCs) and organic/polymer light emitting diodes (O/PLEDs), are so-called surface plasmons (SPs). They are the collective oscillation of electromagnetic waves (EM) and the conduction of electrons at the interface between a metal and dielectric stimulated by an incident of light. With appropriate interface engineering, incident light can be concentrated and confined at the metal/dielectric interface, thereby increasing the absorption. Surface plasmons can be optically excited in metallic nanostructures, namely metallic nanoparticles (NPs) [11-14], highly-

ordered symmetric nanostructures [15-18], and incorporated into metallic nanostructures with electrodes [19-22]. In general, many types of materials, concentrations, shapes, sizes, and distributions have been proposed for PSCs or PLEDs [23-26]. In addition, NPs can be placed outside or inside the active/emissive layer. Improved device performance can be attributed to a strong localized plasmon field improvement, increased light scattering, strong confined field of the localized surface plasmon resonance (LSPR), large density of LSPR, strong exciton-SP coupling or the enhancement in spontaneous emission rate due to the plasmonic near-field effect induced by Au NDs in PSCs and PLEDs, respectively. Instead of embedding NPs into the device, one can also utilize a different technique. This can be done using periodically patterned metallic nanostructures, where light can be effectively coupled to the surface plasmon polariton (SPP) modes. In the former, the excitation of SPP modes can be realized via nanopatterned metallic film as the electrodes. In this case, the enhanced performance was attributed to the LSPR enhancement from the textured electrodes.

Thus, to address poor performance in organic devices (PSCs and PLEDs), we successfully developed a simple technique to incorporate highly ordered nanoimprint gold nanodisks (Au NDs) into active and emissive layers. The incorporated Au NDs enhances the device performance via strong LSPR effect, in which the PCE increased by 14.98% for PSCs. The maximum brightness of plasmonic PLEDs improved from 22730 to 27630 cd/m^2, showing 1.22 times enhancement compared with control PLEDs because of the high density of LSPR, strong exciton-SP coupling and enhancement in spontaneous emission rate due to the plasmonic near-field effect induced by Au NDs. Moreover, the maximum current efficiency of plasmonic PLEDs was enhanced from 16.99 to 19.96 cd/A and has 1.18 times enhancement of that in plasmonic PLEDs.

2 Experimental

1 Materials

Micron-sized graphite powder (1-2 μm, Aldrich) was utilized as the initial precursor for the synthesis of graphene oxide (GO) by a modified Hummers' method [27]. Nitrogen doped Graphene (n-G) was prepared according to the previous report [28]. A 50 mL GO dispersion in ethanol (1 mg/mL) was mixed with 100 mg urea. The mixture was then heated to 80°C and stirred until dried. The dried sample was placed in an Al_2O_3 crucible in the centre of a tube furnace. The furnace was pumped with a rotary pump to 10 Pa and flushed with Ar (100 sccm) to completely remove oxygen gas. After flushing with Ar gas, the temperature of the furnace was raised to 600°C with a heating rate of 3 °C min^{-1} and kept for an hour, and then directly heated up to 900 °C with a heating rate of 5 °C min^{-1}. After 4 hrs of calcination at 900 °C, the furnace was allowed to cool to room temperature before the as-synthesized n-G was collected. We chose n-G to serve as hole buffer layer in both organic devices due to the fact that it shows an excellent catalytic performance in terms of electron transfer [28]. Poly(3,4-ethylenedioxythiophene):poly(4-styrenesulfonate) (PEDOT:PSS) was acquired from H. C. Starck (Germany), polythieno[3,4-b]thiophene/benzodithiophene (PTB7) (M_n = 30000 g/mol) was purchased from 1-Material, [6,6]-phenyl-C_{71}-butyric acid methyl ester ($PC_{71}BM$) was purchased from Electronic Materials (EM) Index Co., Ltd. The nitrogen doped multiwalled carbon nanotubes (n-MWCNTs) were sonicated in chlorobenzene (Sigma Aldrich) overnight and MWCNTs concentrations were controlled with respect to polymers [32]. (4,4-N,N-dicarbazole) biphenyl (CBP) (M_w = 484.59) and tris(2-phenylpyridine) iridium(III) ($Ir(ppy)_3$) (M_w = 654.78) were supplied by Sigma Aldrich. All materials were used without any purification.

2 Preparation of Au nanodisks

The fabrication of the Au NDs begins with patterning the Au NDs array on the ITO-coated glass substrate using a lift-off method, and employing the standard electron beam lithography (EBL) technique (Raith E-Line). The EBL was carried out by exposing a 200 nm thick poly(methyl methacrylate) (PMMA) layer using a pattern of an array of circles. Afterwards, a 5 nm thin Cr and 100 nm Au layer was deposited and finally lift-off process, by means of acetone. It left an array of Au/Cr disks with a height of 100 nm, a diameter of 100 nm (with variance of ~10 nm) and centre to centre separation of 250 nm.

3 PSCs and PLEDs fabrication and characterization

Prior to the patterning of Au NDs (100 nm), the ITO-coated glass substrates were cleaned by an ultrasonic treatment in acetone, methanol, isopropanol, and deionized water sequentially. The pre-cleaned ITO substrates were treated in an ultraviolet-ozone chamber (Ultraviolet Ozone Cleaner, Jetlight Company, USA) for 15 min. Then, an anode interfacial layer, n-doped graphene was deposited at 4000 rpm for 25 s on the ITO electrode from chlorobenzene solution with 1:1.5 wt % (30 nm). The interfacial layer was annealed inside the glove box at 130 °C for 20 min. Later, the photoactive layer was prepared by spin coating (500 rpm) a 1,2-dichlorobenzene solution of PTB7 and a $PC_{71}BM$ (1:1.5 w/w, polymer concentration 12 mg/2 mL^{-1}) on the anode interfacial layer for 25 s. The thickness of the active layer was around 90 nm. The PFN solution was filtered through a 0.45 μm polyvinylidene fluoride (PVDF) filter and spin-coated at 4000 rpm for 25 s on the photoactive layer. The thickness of the PFN was < 5 nm. Finally, the substrate was transferred to a vacuum chamber and 100 nm of Al was thermally deposited on the PFN cathode buffer layer under a base pressure of 1 x 10^{-7} Torr. The active area of the device was 0.04 cm^2.

The power conversion efficiency (PCEs) of the PSCs was measured under an illumination of AM1.5G simulated solar light (Oriel Model 91192) at 100 mW/cm^2. The current density–voltage (J–V) characteristics were recorded with a Keithley 2410 source unit. The external quantum efficiency (EQE) measurements were performed using an EQE system (Model 74000) obtained from Newport Oriel Instruments USA and HAMAMATSU calibrated silicon cell photodiode used as the reference diode. The wavelength was controlled with a monochromator 200-1600 nm. For PSCs, the layers comprised of n-G/Au NDs+PTB7:$PC_{71}BM$:n-MWCNTs/PFN were electrically isolated using toluene and methanol along the perimeter defined by the area of the top electrode. This isolation avoids fringing effects and also prevents over estimation of generated photocurrents. The devices were ITO/n-G/n-doped PTB7:$PC_{71}BM$:n-MWCNTs/PFN/Al and ITO/n-G/Au NDs+PTB7:$PC_{71}BM$:n-MWCNTs/PFN/Al as control and testing devices, respectively.

For the PLEDs, the device structures were ITO/n-G/CBP:$Ir(ppy)_3$/LiF/Al and ITO/n-G/Au NDs+CBP:$Ir(ppy)_3$/LiF/Al as the control and testing device, respectively. A CBP:$Ir(ppy)_3$ solution dissolved in chlorobenzene (0.8 wt%) was spin-cast at 2000 rpm for 45 s on top of the electrodes. Finally, a 1 nm-thin LiF layer and a 100 nm-thick Al layer were thermally evaporated on top of the CBP:$Ir(ppy)_3$ layer. The current density-voltage (J-V), luminance-voltage (L-V), EL spectrum and EQE characteristics were measured using a Konica Minolta CS100A luminance meter and CS1000A spectrometer coupled with a Keithley 2635A voltage and current source meter.

3 Results and discussion

The UV–Vis absorption spectrum of the Au NDs in aqueous solution is shown in Fig. 1. The average diameter of the Au ND was approximately 100 nm with uniformly-sized distributions as illustrated by scanning electron microscopy (SEM) (Fig. 1). The UV–Vis spectrum of the Au NDs solution peaks at 550 nm, indicating the presence of a plasmon absorption band (Fig. 1). Spectral overlap (Fig. 2a) between an absorption spectrum of PTB7:PC_{71}BM:n-MWCNTs (400–650 nm) and plasmon region of the Au NDs (540 nm) can be achieved. Accordingly the efficient plasmonic near the field excitation enhancement is expected.

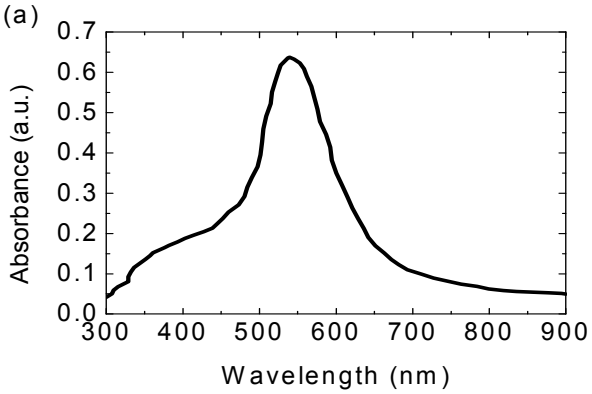

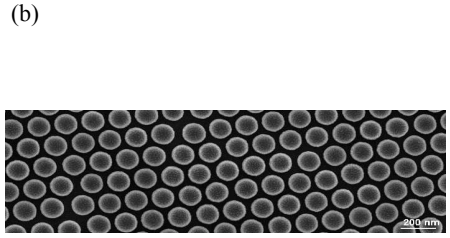

Fig. 1. (a) Absorption spectrum, and (b) SEM image of the Au ND.

The UV–Vis absorption spectrum of the Au NDs in aqueous solution is shown in Fig. 1. The average diameter of the Au ND was approximately 100 nm with uniformly-sized distributions as illustrated by scanning electron microscopy (SEM) (Fig. 1). The UV–Vis spectrum of the Au NDs solution peaks at 550 nm, indicating the presence of a plasmon absorption band (Fig. 1). Spectral overlap (Fig. 2a) between an absorption spectrum of PTB7:PC_{71}BM:n-MWCNTs (400–650 nm) and plasmon region of the Au NDs (540 nm) can be achieved. Accordingly the efficient plasmonic near the field excitation enhancement is expected.

Fig. 2a demonstrates absorption spectra of PTB7:PC_{71}BM:n-MWCNTs thin films on n-G coated quartz substrates with and without Au NDs. One can clearly observe absorbance enhancement after the integration of Au NDs in the region of 420 until 600 nm. In the spectral range of 300–700 nm where the PTB7:PC_{71}BM:n-MWCNTs film absorbs, ~14% enhancement in the absorbance intensity of the PTB7:PC_{71}BM:n-MWCNTs was documented, corresponding to the increased electric field in the active layer by the excited LSPR from the Au NDs. It is clear that the plasmon region of the Au NDs matches the absorption spectrum of PTB7:PC_{71}BM:n-MWCNTs, the absorbance intensity of PTB7 with Au NDs increases, which may be ideal for the enhancement of the J_{SC} upon fabricating the plasmonic solar cell.

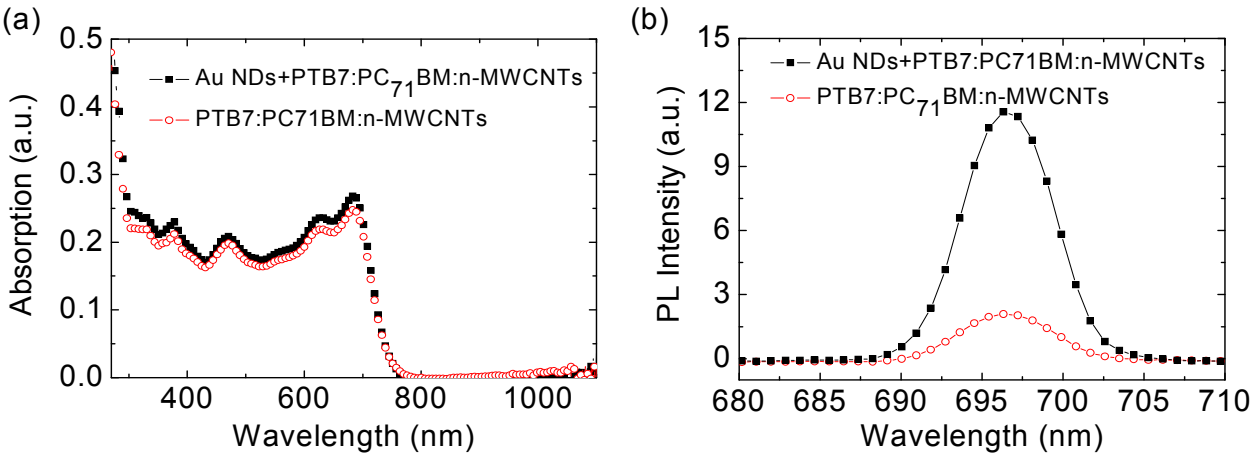

Fig. 2. (a) Absorption, and (b) PL spectra of PTB7:PC_{71}BM:n-MWCNTs and Au NDs+PTB7:PC_{71}BM:n-MWCNT

The PL spectra of PTB7:PC_{71}BM:n-MWCNTs thin films on n-G coated quartz substrates with and without Au NDs are illustrated in Fig. 2b. A similar trend is seen from the PL spectra where the spectrum of PTB7:PC_{71}BM:n-MWCNTs with Au NDs is significantly stronger than that of the PTB7:PC_{71}BM:n-MWCNTs without the presence of Au NDs. The presence of Au NDs induced an increment of about 5.52 times in the PL intensity. This corresponds to the propagating plasmonic field leading to enhancement in the radiative relaxation of the electronic states in the conjugated polymer [29,30]. Hence, the propagating oscillation of the surface plasmon dipole generated a strong coupling between the excitonic state of PTB7:PC_{71}BM:n-MWCNTs and the plasmonic

field of the Au NDs. Consequently it enhanced the PL intensity in the Au NDs+PTB7:$PC_{71}BM$:n-MWCNTs.

Table 1. Photovoltaic parameter based on PTB7:$PC_{71}BM$:n-MWCNTs.

Device	J_{SC} (mA/cm^2)	V_{OC} (V)	FF (%)	PCE (%)
Control	17.05±0.10	0.74±0.01	64.01±0.02	8.08±0.03
Plasmonic	19.10±0.12	0.74±0.01	65.76±0.03	9.29±0.01

To access in detail the influence of the Au NDs on the photovoltaic performance, we fabricated two sets of PSCs. The plasmonic and control devices are ITO/n-G/PTB7:$PC_{71}BM$:n-MWCNTs+Au NDs/PFN/Al and ITO/n-G/PTB7:$PC_{71}BM$:n-MWCNTs/PFN/Al, respectively. Fig. 3 demonstrates the current density–voltage (J–V) characteristics of the fabricated devices under AM1.5G illumination at 100 mW/cm^2. Fig. 3a illustrates the J-V characteristics of the devices in the dark along with high rectification of about 10^4 at ± 1 V. High rectification can be attributed to a few shortcomings or pin holes in these devices. The unchanged in the J-V curves also illustrates total series resistance (R_s) of the diode devices did not decay with the integration of Au NDs [31].

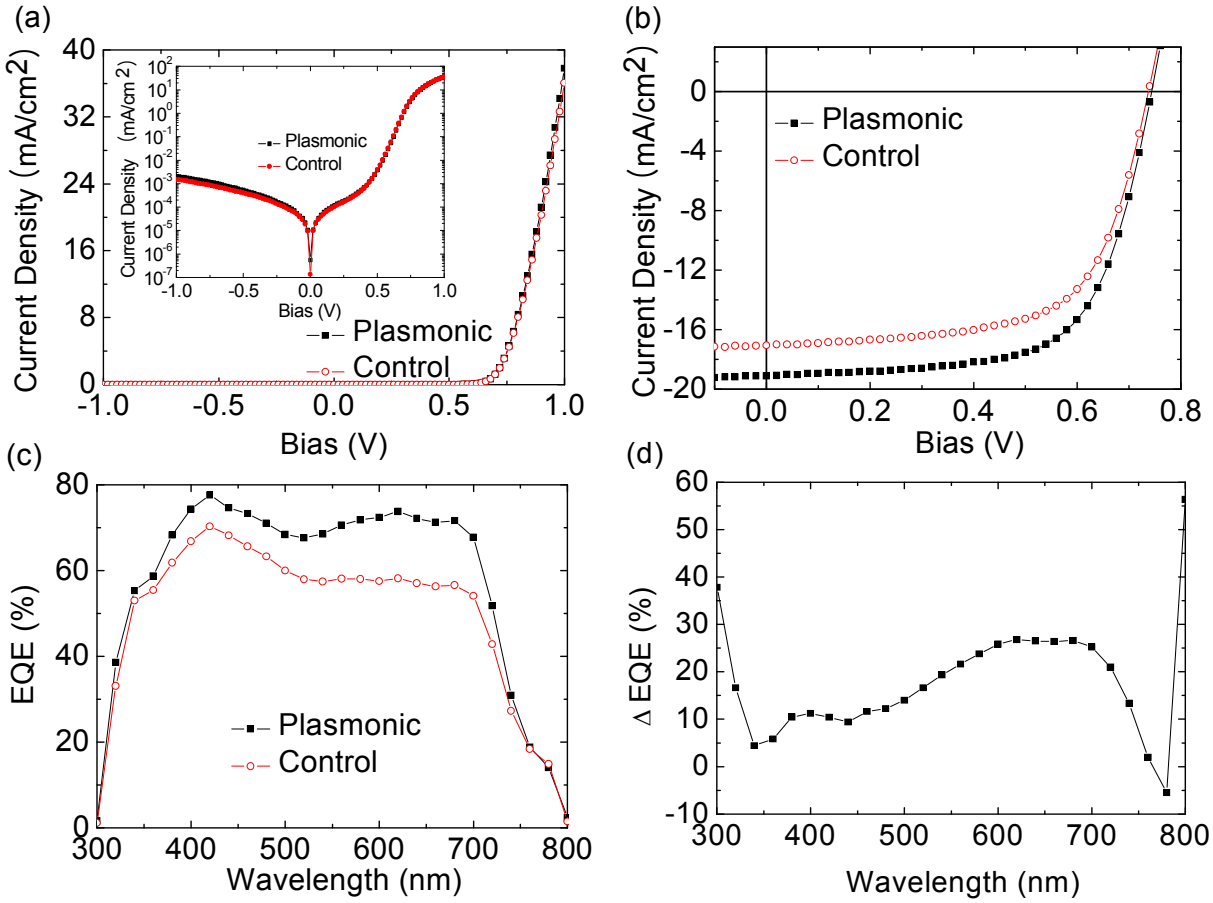

Fig. 3. (a) Dark J-V characteristics, (b) J-V characteristics measured under AM1.5G illumination at 100 mW/cm^2, (c) EQE spectra, and (d) ΔEQE enhancement plot.

Fig. 3b depicts the J-V characteristics of two different devices under 100 mW/cm^2 of AM1.5G irradiation. Table 1 collects the photovoltaic parameters. The results represent the average values calculated over 43 devices. The control devices (red circle) exhibit an open circuit voltage (V_{oc}) of 0.74 V, a J_{sc} of 17.05 mA/cm^2, a fill factor (FF) of 64.01%, and a PCE of 8.08%. It is worth noting that our approach uses n-G as an anode interfacial layer. It has a slightly low performance compared to the previously published work by Lu [32]. In their system, they obtained a significantly higher FF despite a remarkable loss in the V_{oc} leading to 8.6% PCE [32]. On the other hand, upon the integration of Au NDs, our plasmonic solar cells exhibited similar V_{oc} of 0.74 V, a J_{SC} of 19.10 mA/cm^2, a FF of 65.76%, corresponding to a drastic improvement of 9.29% PCE.

There was a 12.02% improvement in J_{SC} when the Au NDs were integrated into the devices. Compared to the control devices, it is consistent with the absorption enhancement. In accordance to the Mie theory [32], the total extinction coefficient represents the total losses of energy from the incident light due to both absorption and scattering and is defined as the summation of both absorption and scattering components related with each supported SPs mode of particle. In the case of large Au NDs, the total extinction cross section consists of a large scattering and small absorption cross sections. When Au NDs are incorporated into a device, it scatters light into the active layer, leading to the improved coupling of incident light and a far-field scattering plasmon wave [33,34]. Moreover, these SPs also generate large local electromagnetic fields near the nanoparticle surface [35-37], in which it will eventually increase the light absorption as well as the PCE [38-40].

Fig. 3c demonstrates the external quantum efficiency (EQE) spectra of control and plasmonic devices. The plasmonic devices exhibit higher EQE than that of the control device in the whole visible regime, which elucidates significantly higher J_{SC} than observed in the plasmonic. The EQE enhancement from 300 – 750 nm is consistent with the absorption enhancement shown in Fig. 2a. In general, the EQE depends proportionally on the absorption efficiency of the PSC, we attribute the J_{SC} enhancement to a combination of improved optical path length in the polymer thin films, due to the light scattering by the Au NDs, and plasmonic near-field absorption enhancement effects.

Moreover, the calculated relative improvement, as a function of wavelength, is depicted in Fig. 3d. It is clear that there is remarkable improvement coinciding with the SPR peak of Au NDs (Fig. 1a). This observation complies with the improved J_{SC}.

In general, the presence of the surface plasmon field, due to the presence of the Au NDs, facilitated the absorption of the active layer, and increased the rate of exciton generation. Furthermore it facilitated the probability of exciton dissociation into free charge carriers [38], where the enhanced probability of exciton dissociation leads to a decrease in recombination rate. Hence, we attribute a ~2.73% enhancement in the FF value to the light scattering from the Au NDs. The improved exciton generation rate, as well as efficient exciton dissociation probability, was induced by the local enhancement in the electromagnetic field originating from excitation of the LSPR. Therefore, the PSCs integrated with Au NDs exhibited superior performance than the control device.

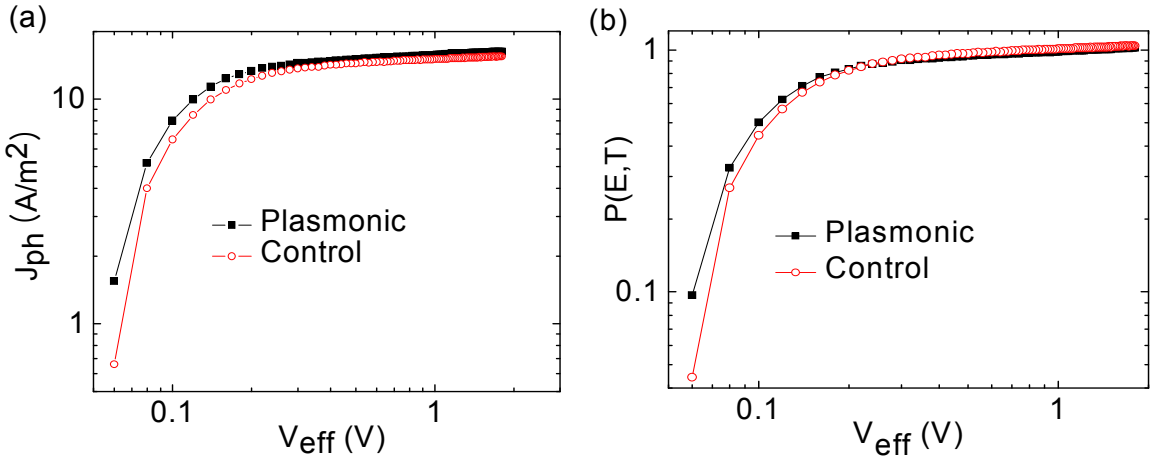

Fig. 4. (a) Photocurrent density versus effective voltage, and (b) exciton dissociation probability versus effective voltage for control and plasmonic devices

The influence of Au NPs on exciton generation and dissociation behaviours was further studied. We calculated the maximum exciton generation rate (G_{max}) and exciton dissociation probability P(E,T) of the plasmonic and control devices. The devices were biased, ranging from +1 V to -1 V. Fig. 4a exhibits the photocurrent density (J_{ph}) versus the internal voltage (V_{int}) for both devices, under illumination at 100 mW/cm^2 of AM1.5G. The J_{ph} is denoted as:

$$J_{ph} = J_L - J_D \quad (1)$$

where J_L and J_D are the current densities under illumination and in the dark, respectively. The V_{int} is denoted as:

$$V_{int} = V_{BI} - V_{app} \quad (2)$$

where V_{BI} and V_{app} are the voltage at which $J_{ph} = 0$, and the applied voltage, respectively. From Fig. 4, there are two distinguishable regimes; low and high V_{int}. The J_{ph} increased in proportion to the voltage (in the low V_{int}), whereas the J_{ph} saturated with increased voltage (the high V_{int}), where the internal field is high enough to sweep out all dissociated charge carriers to the respective electrodes. Therefore, the J_{ph} saturated is confined to the number of absorbed photons. In assuming that the saturated J_{ph} is independent of the bias and temperature, we attained the G_{max} using the following equation:

$$J_{ph} = qLG_{max} \quad (3)$$

where q is the electronic charge, and L is the thickness of the active layer [41,42], assuming that all of the generated excitons dissociated into holes, and electrons and contributed to the current in the saturated regime. The G_{max} for the plasmonic and control devices is 5.17×10^{27} m^{-3} s^{-1} ($J_{ph,sat}$ = 114 A/m^2), and 5.46×10^{27} m^{-3} s^{-1} ($J_{ph,sat}$ = 127 A/m^2), respectively. The increased G_{max} value reveals that the integration of Au NDs significantly improved light absorption, exciton generation rate, and exciton dissociation probability. Note that G_{max} has the maximum photoinduced carrier generation rate per unit volume [41,42]. Next, we determined the exciton dissociation probability for both devices; which is related to the electric field (E) and temperature (T). Due to the fact that only a fraction of the generated excitons can be dissociated into free carriers, the J_{ph} can also be written as [41,42]

$$J_{ph} = qG_{max}P(E,T)L \quad (4)$$

The P(E,T) can be determined by normalizing the J_{ph} with saturated J_{ph} (J_{ph}/J_{sat}) [43]. From Fig. 4b, one can obviously see the improvement of the P(E,T) under the short-circuit conditions (V_a = 0 V) from 80 to 89% for the control and plasmonic devices, respectively. This indicates that the excitation of the LSPR caused generated excitons to dissociate into free carriers. Consequently, it is concluded that the excitation of the LSPR not only improved the

exciton generation rate but also the exciton dissociation probability and improved the J_{SC} of the PSCs.

To further extend our investigation on the charge recombination kinetics, we analyzed a variation of J_{SC} on our fabricated plasmonic devices as a function of light intensity (25 to 100 mW/cm^2 in steps of 5 mW/cm^2). Several research groups have suggested a power law dependence of J_{SC} on light intensity by the following equation [41,44].

$$J_{sc} \propto I^{\alpha} \quad (5)$$

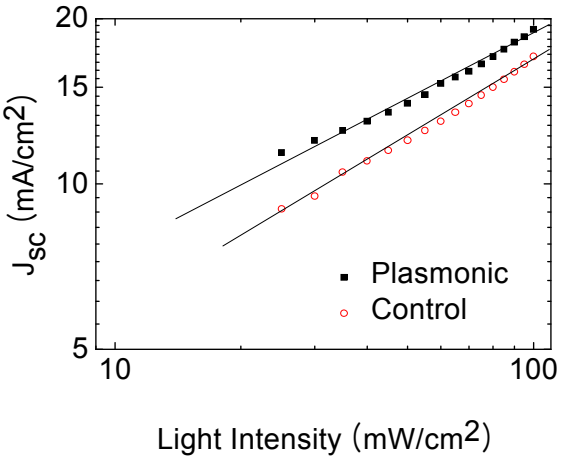

Fig. 5. Current density (J_{SC}) versus light intensity.

Fig. 5 demonstrates the variation of J_{SC} as a function of light intensity in a log-log scale, and fitted to a power law using equation 5. As shown in Fig. 5, the linear dependence of J_{SC} is consistent with the sweep-out at short circuit, and this shows that bimolecular recombination is insignificant [45]. The α for the plasmonic and control devices is 0.992, and 0.983, respectively. Accordingly, we anticipate that the integration of Au NDs into the PTB7:PC_{71}BM:n-MWCNTs has an unimportant effects on the charge transport process in the device.

Despite recent advancement in PSCs, stability and lifetime are still one of the biggest issues. Different approaches have been previously reported in order to overcome the aforementioned problems including i) employing an inverted architecture, and ii) using metal-oxide transition materials, which are relatively stable toward the environment. We performed stability measurements for our devices over one month. Fig. 6 shows the PCE as a function of time. J-V characteristics were measured every week under simulated AM1.5 solar irradiation (100 mW/cm^2). It is worth noting that the V_{OC} of both devices remain stable throughout the stability measurement. Control devices, for instance (not shown) the J_{SC} decreased slightly after the first week, although the FF dropped remarkably. The J_{SC} began to decrease during the second week, where the J_{SC} dropped from 16.97 to 15.11 mA/cm^2. The efficiency of the control device dropped remarkably, after the fourth week measurement, to 5.36%; which is a 33.66% decrease. Compared to control devices, plasmonic devices also suffered some degradation over 4 weeks, where the PCE decreased to 7.1% after four weeks of measurements. This is due to the significant decrease of J_{SC} and FF during the four weeks of measurements. The efficiency dropped almost 23.57% from its initial value.

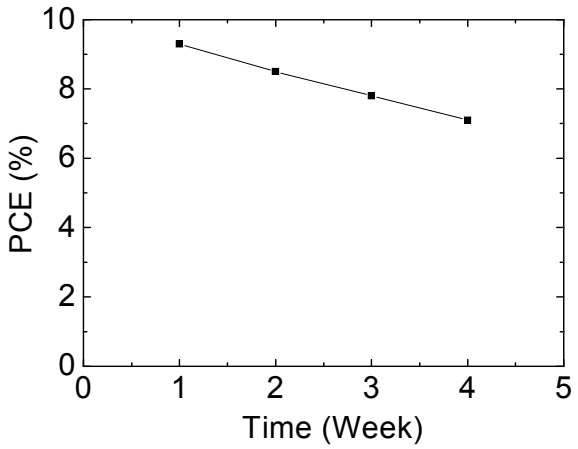

Fig. 6. Lifetime measurements of the plasmonic devices over 4 weeks under ambient air.

Despite recent advancement in PSCs, stability and lifetime are still one of the biggest issues. Different approaches have been previously reported in order to overcome the aforementioned problems including i) employing an inverted architecture, and ii) using metal-oxide transition materials, which are relatively stable toward the environment. We performed stability measurements for our devices over one month. Fig. 6 shows the PCE as a function of time. J-V characteristics were measured every week under simulated AM1.5 solar irradiation (100 mW/cm^2). It is worth noting that the V_{OC} of both devices remain stable throughout the stability measurement. Control devices, for instance (not shown) the J_{SC} decreased slightly after the first week, although the FF dropped remarkably. The J_{SC} began to decrease during the second week, where the J_{SC} dropped from 16.97 to 15.11 mA/cm^2. The efficiency of the control device dropped remarkably, after the fourth week measurement, to 5.36%; which is a 33.66% decrease. Compared to control devices, plasmonic devices also suffered some degradation over 4 weeks, where the PCE decreased to 7.1% after four weeks of measurements. This is due to the significant decrease of J_{SC} and FF during the four weeks of measurements. The efficiency dropped almost 23.57% from its initial value.

To further support our observations, we fabricated PLEDs using n-G as the hole injection material and CBP:Ir(ppy)$_3$ as an emissive material. The plasmonic and control architectures are ITO/n-G/CBP:Ir(ppy)$_3$+Au NDs/LiF/Al and ITO/n-G/CBP:Ir(ppy)$_3$/LiF/Al, respectively. The J-V characteristics of plasmonic and control devices are compared in Fig. 7a, in which the PSCs with Au NDs exhibit remarkable effects in the device performance. The current density of the plasmonic PLEDs is significantly higher at the same voltage (6 – 12 V) in contrast to the control PLEDs. The current efficiency (CE), at a current density of 6.6 mA/cm^2 for plasmonic PLEDs (20 cd/A), shows a 17.65% improvement compared to the control PLEDs (17 cd/A) (Fig. 7b). Meanwhile, as depicted in Fig. 7c, the luminance of 5000 cd/m^2 at a current density of 31.16 mA/cm^2 is obtained for plasmonic PLEDs, which is improved significantly relative to that of control PLEDs, 26.04 mA/cm^2. This substantial performance improvement in plasmonic PLEDs is related to the Au NDs, which can cause LSPR and light scattering enhancement. Table 2 summarizes all parameters for PLEDs based on the CBP:Ir(ppy)$_3$ host guest matrix.

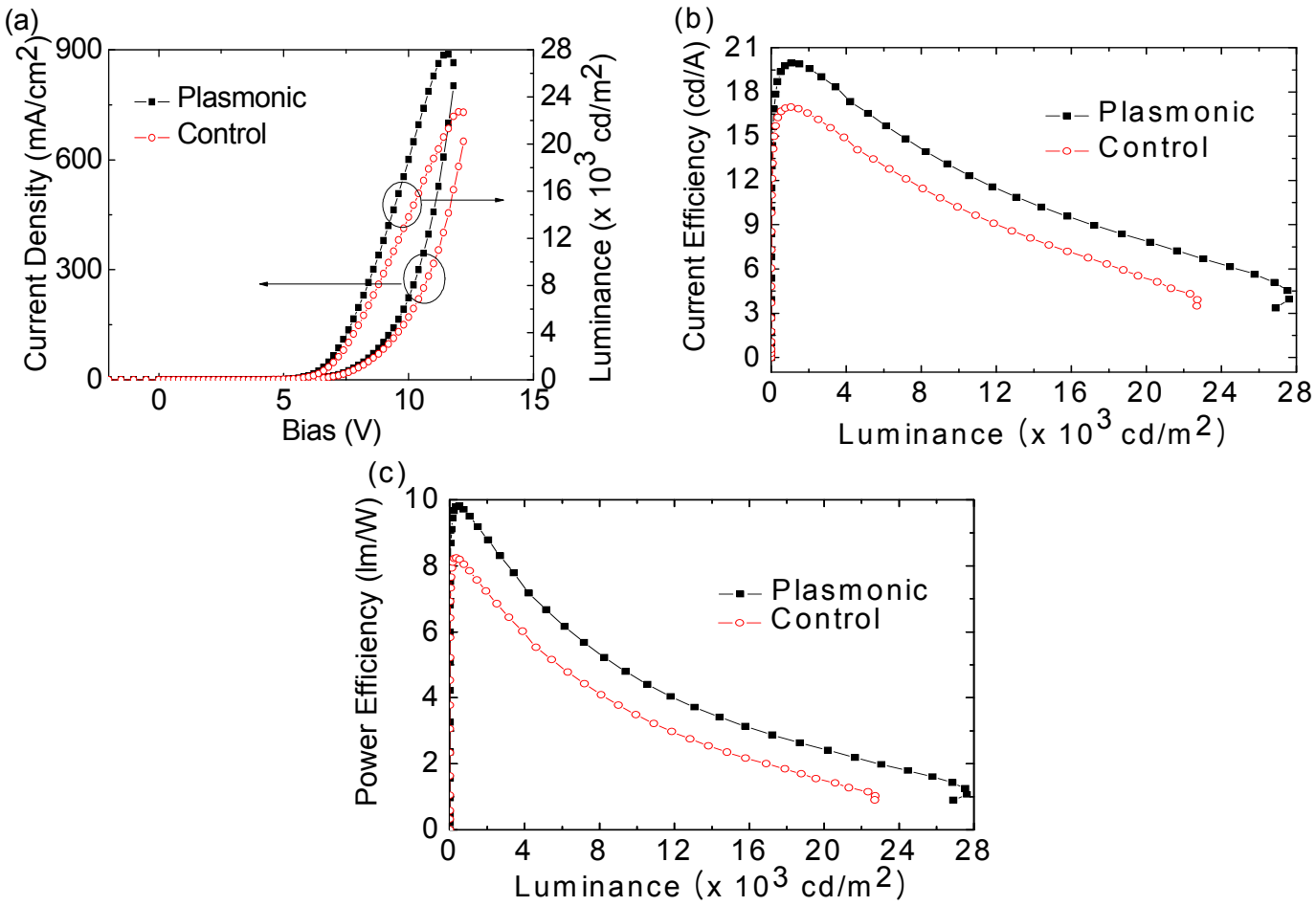

Fig. 7. PLEDs characteristics. (a) Current density vs. bias vs. luminance, (b) current efficiency vs. luminance, and (c) power efficiency vs. luminance.

Table 2. Device performance of PLEDs based on CBP:Ir(ppy)$_3$ host guest matrix.

Substrate	V_T(V)	V_D(V)	Maximum		@1000(cd/m^2)		L_{max} (cd/m^2)
			C/E (cd/A)	P/E (lm/W)	C/E (cd/A)	P/E (lm/W)	
Control	3.13	5.58	16.99	8.24	16.97	7.89	22730
Plasmonic	3.07	5.42	19.96	9.82	19.92	9.55	27630

It has been proposed that one of the main contributing factors for improved performance in organic devices induced by metal nanoparticles is due to the presence of a strong interaction between the LSPR and excitons [46]. Thus to probe this issue, we performed time-resolved photoluminescence (TRPL) measurements (Fig. 8). The excitation wavelength used is 486 nm, and the PL decay is fitted using the following equation:

$$I_{PL}(t) = \sum_{i=1}^{n} A_i \exp\left(-t/\tau_i\right) \qquad (6)$$

where A_i is the amplitude of the i_{th} decay, n is the number of decays and τ_i is the exponential constant of the i_{th} decay. The exciton lifetime for plasmonic PLEDs (1.38 ns) significantly decreases in contrast to the control PLEDs (1.89 ns). The strong reduction suggests that the enhanced spontaneous emission rate of CBP:Ir(ppy)$_3$ is induced by LSPR on Au NDs.

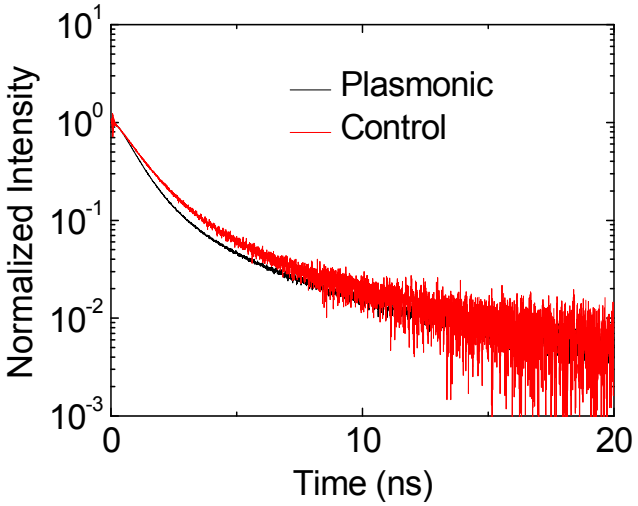

Fig. 8. Time-resolved PL spectra detected at 518 nm wavelength excited by a 486 nm laser source.

The PL lifetime of the excited state is inversely proportional to the probability that the molecule will transit back to the ground state. Thus, the embedded Au NDs inside the emissive layer decreases the lifetime of the excited state of emissive material. To fully understand the PL decay rate, radiative and nonradiative recombination rate of excitons should be taken into account as $\Gamma_{tot} = \Gamma_{rad} + \Gamma_{non\ rad}$. In PLEDs, when electrons and holes are injected respectively from the cathode and anode into the emissive layer by a bias voltage, these two types of carriers migrate towards each other and a fraction of them recombine to form excitons and emit light upon radiative decay. The formed excitons relax according to the radiative (Γ_{rad}) and nonradiative ($\Gamma_{non\ rad}$) recombination rates. The internal quantum efficiency (IQE) is defined as:

$$IQE = \frac{\Gamma_{rad}}{\Gamma_{tot}} = \frac{\Gamma_{rad}}{\Gamma_{rad} + \Gamma_{non}} \quad (7).$$

For plasmonic PLEDs, when Au NDs grow inside the emissive layer, and the emission wavelength of emissive layer is close to the LSPR wavelength, the exciton energy transfers between the exciton and SP through the exciton-SP coupling rate (Γ_{spc}). The PL decay rate increases to Γ_{tot}^* by the SP coupling rate as $\Gamma_{tot}^* = \Gamma_{rad} + \Gamma_{non\ rad} + \Gamma_{spc}$ and the enhanced IQE can be defined as:

$$IQE^* = \frac{\Gamma_{rad} + \Gamma_{spc}}{\Gamma_{rad} + \Gamma_{non} + \Gamma_{spc}} \quad (8).$$

In addition, the cylindrical shape of the Au NDs leads in high electromagnetic fields distribution around Au NDs and the scattering of SPs of high momentum SPs. Consequently it is beneficial to the extraction of the SP energy and therefore increases Γ_{spc}. The increment of Γ_{spc} relatively causes the PL decay rates to improve since the Γ_{spc} value is expected to be very fast. This indicates that the SP coupling can improve the IQE. However, the Γ_{spc} can be disadvantageous due to the fact the SP is a non-propagating evanescent wave, which makes it difficult to extract light from the SPP mode. For instance, the SP energy will be thermally scattered in various directions if the metal surface is perfectly flat. Despite that, the SP energy would be thermally dissipated. The SPP energy can also be extracted and made radiative by utilizing metallic nanostructures or roughness. Such metallic nanostructure or roughness allows SPs along with high momentum to disperse, lose momentum and to couple to radiative light. In our study, the metallic nanostructure of Au NDs makes the SPs decay radiatively.

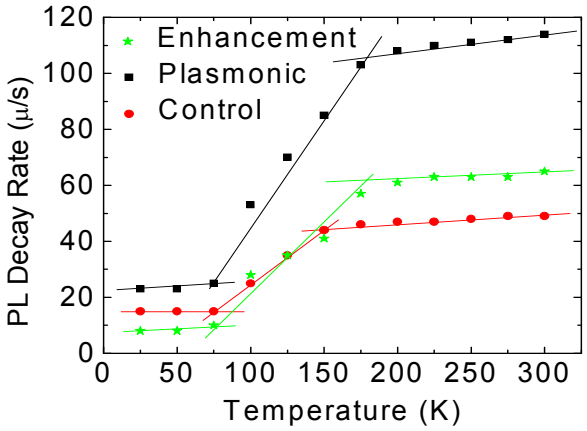

Fig. 9. PL decay rates of our fabricated PLEDs including its differences as a function of temperature.

To further analyze the Γ_{spc} in our fabricated PLEDs, we extended our measurements by evaluating temperature dependency of TRPL. In brief, there are two possible mechanisms that could possibly cause the observed temperature effects namely i) electron-phonon scattering in the Au NDs, and ii) thermal expansion of the Au NDs. The first argument shows the phonon populations in Au NDs increase with the increase of temperature. This leads to the improved probability of electron-phonon scattering, and subsequently increased the scattering rate of the electrons. The temperature dependence of the scattering rate of the electrons can be defined as:

$$\gamma_\infty(T) = K'T^5 \int_0^{\frac{\theta}{T}} \frac{z^4 dz}{e^z - 1} \quad (9)$$

where θ is the Debye temperature for Au, K' is a constant.

Meanwhile, the second argument is based on thermal expansion of the Au NDs, in which the volume of the Au NDs increases with the temperature:

$$V(T) = V_0(1 + \beta\Delta T) \quad (10)$$

where $\Delta T = T - T_0$ is the changes in temperature, β is the volume thermal expansion coefficient, and V_0 is the volume of Au NDs. Accordingly, the SP resonance energy can be defined as:

$$\omega_{sp} = \sqrt{\frac{\omega_{p0}^2}{(1 + 2\varepsilon_m + \varepsilon_{ib1})(1 + \beta\Delta T)} - \gamma^2} \quad (11)$$

where $\omega_{p0} = \sqrt{\frac{4\pi n_0 e^2}{m^*}}$ is the bulk plasmon at room temperature, ε_m is the dielectric permittivity, and ε_{ib} is the contribution of the interband transitions in the dielectric permittivity of Au. The thermal expansion of Au NDs leads to the decrease of the free electrons concentration in Au NDs, where the Au NDs thermal expansion would influence the frequency of SP resonance through the frequency of bulk plasmon.

Fig. 9 demonstrates the PL decay rates of the plasmonic and control PLEDs versus temperature. There are three distinguishable regimes: low, medium and high temperatures. PL decay rates revealed that in both type of devices, the decay rate is almost unchanged at the lower temperature regime (below 100 K). Meanwhile in the medium temperature, up to 200 K, the PL decay rates enhance linearly with temperature. For higher temperature regime, the PL decay rates tend to saturate. Big differences in PL decay rates of the plasmonic and control PLEDs corresponding to exciton-SP coupling is likely to be more efficient at higher temperatures. Moreover, the calculated differences of PL decay rates as a function of temperature (green stars), suggests that phonon also does play an important role in the SP coupling.

Conclusions

In summary, we have successfully demonstrated the significantly enhanced performances of PSCs and PLEDs by integrating Au NDs into these devices. The PSC devices based on PTB7:PC_{71}BM:N-MWCNTs+Au NDs, exhibited a 14.98% improvement in device efficiency (8.08% and 9.29% for control and plasmonic devices,

respectively), whereas the power efficiency of the PLEDs improved by 78.16% (2.93 to 5.22 lm/W for control and plasmonic devices, respectively). The LSPR and enhanced light scattering obviously contributed to the enhanced performance. It is also found that the excitons-SP coupling is strongly dependent on temperature. This clearly suggests that metal nanoparticles can be fully utilized for organic devices for further enhancement.

Acknowledgements

The authors would also like to thank MOHE, National University of Malaysia and University of Malaya for providing financial assistance with grant number ICONIC-2013-005 and FP033 2013A, respectively. This work was also supported by CAPES-PNPD Project No. 3076/2010 and Human Resources Development program (No. 20134010200490) of the Korea Institute of Energy Technology Evaluation and Planning (KETEP) grant funded by the Korea government Ministry of Trade, Industry and Energy.

Notes and references

[a]*Solar Energy Research Institute, National University of Malaysia, 43600 Bangi, Selangor, Malaysia Fax: +603 8911 8574; Tel: +603 8911 8580; E-mail: asri@ukm.edu.my*.
[b]*Department of Chemistry, University of Malaya, Kuala Lumpur 50603, Malaysia Fax: +603 7967 4193; Tel: +603 7967 4082; E-mail: jeff@um.edu.my*.
[c]*Universidade Tecnologica Federal do Parana, GPGEI – Av. Sete de Setembro, 3165 – CEP 80230-901 – Curitiba, Parana, Brasil; Fax: +55 41 331 04691; Tel: +55 41 331 04691; E-mail: wjsilva2000@yahoo.com.br*.
[d]*Department of Information, Display and Advanced Display Research Center, Kyung Hee University, Dongdaemun-ku, Seoul 130-171, Republic of Korea. Fax: +82 2 961 0270; Tel: +82 2 961 0270; E-mail: abdr@khu.ac.kr; jjang@khu.ac.kr.*

1 W. J. da Silva, H. P. Kim, A. R. B. M. Yusoff, and J. Jang, *Nanoscale*, 2013, **5**, 9324.
2. A. R. B. M. Yusoff, D. Kim, H. P. Kim, F. K. Shneider, W. J. da Silva, and J. Jang, *Energy & Environ. Sci*, 2015, **8**, 303.
3. A. R. B. M. Yusoff, S. J. Lee, H. P. Kim, F. K. Shneider, W. J. da Silva, and J. Jang, *Adv. Funct. Mater.*, 2014, **24**, 2240.
4. http://www.nrel.gov/ncpv/images/efficiency_chart.jpg.
5. K. T. Kamtekar, A. P. Monkman, and M. R. Bryce, *Adv. Mater.*, 2010, **22**, 572.
6. S. A. Jenekhe, *Nat. Mater.*, 2008, **7**, 354.
7. X. Gong, S. Wang, D. Moses, G. C. Bazan, and A. J. Heeger, *Adv. Mater.*, 2005, **17**, 2053.
8. Y. Zhang, F. Huang, Y. Chi, and A. K. -Y. Jen, *Adv. Mater.*, 2008, **20**, 1565.
9. D. Kabra, L. P. Lu, M. H. Song, H. J. Snaith, and R. H. Friend, *Adv. Mater.*, 2010, **22**, 3194.
10. D. Kabra, M. H. Song, B. Wenger, R. H. Friend, and H. J. Snaith, *Adv. Mater.*, 2008, **20**, 3447.
11. A. J. Morfa, K. L. Rowlen, T. H. Reilly, M. J. Romero, and J. van de Lagemaat, *Appl. Phys. Lett.*, 2008, **92**, 013504.
12. S. –S. Kim, S. –I. Na, J. Jo, D. –Y. Kim, and Y. –C. Nah, *Appl. Phys. Lett.*, 2008, **93**, 073307.
13. J. H. Lee, J. H. Park, J. S. Kim, D. Y. Lee, and K. Cho, *Org. Electron.*, 2009, **10**, 416.
14. F. C. Chen, J. L. Wu, C. L. Lee, Y. Hong, C. H. Kuo, M. H. Huang, *Appl. Phys. Lett.*, 2009, **95**, 013305.
15. X. H. Li, W. E. I. Sha, W. C. H. Choiy, D. D. S. Fung, and F. X. Xie, *J. Phys. Chem. C*, 2012, **116**, 7200.
16. J. Hou, X. Li, F. Xie, W. E. I. Sha, J. H. Kwong, G. Li, W. C. H. Choy, and Y. Yang, *Adv. Energy Mater.*, 2012, **2**, 1203.
17. R Dunbar, H. Hesse, D. Lembke, and L. S. –Mende, *Phys. Rev. B*, 2012, **85**, 035301.
18. A. E. Ostfeld, and D. Pacifici, *Appl. Phys. Lett.*, 2011, **98**, 113112.
19. M. G. Kang, M. S. Kim, J. Kim, and L. J. Guo, *Adv. Mater.*, 2008, **20**, 4408.
20. M. G. Kang, T. Xu, H. J. Park, X. Luo, and L. J. Guo, *Adv. Mater.*, 2010, **22**, 4378.
21. E. C. Garnett, W. Cai, J. J. Cha, F. Mahmood, S. T. Connor, M. G. Christoforo, Y. Cui, M. D. McGehee, and M. L. Brongersma, *Nat. Mater.*, 2012, **11**, 241.
22. N. C. Lindquist, W. A. Luhman, S. H. Oh, and R. J. Holmes, *Appl. Phys. Lett.*, 2008, **93**, 123308.
23. W. Sha, W. Choy, Y. Liu, and W. Chew, *Appl. Phys. Lett.*, 2011, **99**, 113304.
24. D. Qu, F. Liu, Y. Huang, W. Xie, and Q. Xu, *Opt. Express*, 2011, **19**, 24795.
25. R. Dunbar, T. Pfadler, and L. S. –Mende, *Opt. Express*, 2012, **20**, A1777.
26. I. Kim, T. S. Lee, D. S. Jeong, W. S. Lee, and K. S. Lee, *J. Phys. D:Appl. Phys.*, 2012, **45**, 065101.
27. M. Sookhakian, Y. Amin, S. Baradaran, M. Tajabadi, A. M. Golsheikh, W. Basirun, *Thin Solid Films*, 2014, **552**, 204.
28. J. Jin, X. Fu, Q. Liu, Y. Liu, Z. Wei, K. Niu, J. Zhang, *ACS Nano*, 2013, **7**, 4764.
29. J. Pei, J. Tao, Y. Zhou, Q. Dong, Z. Liu, Z. Li, F. Chen, J. Zhang, W. Xu, and W. Tian, *Sol. Energy Mater. Sol. Cells*, 2011, **95**, 3281.
30. M. Niggeman, M. Riede, A. Gombert, and K. Leo, *Phys. Status Solidi A*, 2008, **205**, 2862.
31. J. H. Lee, J. H. Park, J. S. Kim, D. Y. Lee, and K. Cho, *Org. Electron.*, 2009, **10**, 416.
32. L. Lu, T. Xu, W. Chen, J. M. Lee, Z. Luo, I. H. Jung, H. I. Park, S. O. Kim, and L. Yu, *Nano Lett.*, 2013, **13**, 2365.
33. J. R. Lakowicz, *Anal. Biochem.*, 2005, **337**, 171.
34. W. A. Murray, and W. L. Barnes, *Adv. Mater.*, 2007, **19**, 3771.
35. M. Moskovits, *J. Raman Spectrosc.*, 2005, **36**, 485.
36. W. Leng, H. Y. Woo, D. Vak, G. C. Bazan, and A. M. Kelley, *J. Raman Spectrosc.*, 2006, **37**, 132.
37. C. L. Haynes, and R. P. van Duyne, *J. Phys. Chem. B*, 2003, **107**, 7426.
38. F. –C. Chen, J. –W. Wu, C. –L. Lee, Y. Hong, C. -H. Kuo, and M. H. Huang, *Appl. Phys. Lett.*, 2009, **95**, 013305.
39. A. P. Kulkarni, K. M. Noone, K. Munechika, S. R. Guyer, and D. S. Ginger, *Nano Lett.*, 2010, **10**, 1501.
40. A. J. Morfa, K. L. Rowlen, T. H. Reilly, M. J. Romero, and J. van de Lagemaat, *Appl. Phys. Lett.*, 2008, **92**, 013504.
41. V. D. Mihailetchi, H. X. Xie, B. de Boer, L. J. A. Koster, and P. W. M. Blom, *Adv. Funct. Mater.*, 2006, **16**, 699.
42. V. D. Mihailetchi, L. J. A. Koster, J. C. Hummelen, and P. W. M. Blom, *Phys. Rev. Lett.*, 2004, **93**, 216601.
43. V. Shrotriya, Y. Yao, G. Li, and Y. Yang, *Appl. Phys. Lett.* 2006, **89**, 063505
44. P. Schilinsky, C. Waldauf, and C. J. Brabec, *Appl. Phys. Lett.*, 2002, **81**, 3885.

45. V. Shrotriya, E. H. E. Wu, G. Li, Y. Yao, and Y. Yang, *Appl. Phys. Lett.*, 2006, **88**, 064104.
46. X. Ma, J. Benavides, C. R. Haughn, F. Xu, M. F. Doty, and S. G. Cloutier, *Org. Electron.*, 2013, **14**, 1916.

